A Physical Layer for Low Power Optical Wireless Communications

Malte Hinrichs, *Member, IEEE*, Pablo Wilke Berenguer, Jonas Hilt, Peter Hellwig, Dominic Schulz, Anagnostis Paraskevopoulos, *Member, IEEE*, Kai Lennert Bober, Ronald Freund, and Volker Jungnickel, *Member, IEEE*

***Abstract*—Energy consumption is one of the critical issues in optical wireless communications transmitter design and a limiting factor to miniaturization and deployment in mobile devices. In order to reduce energy requirements, we assess a physical layer based on high-bandwidth on-off keying modulation. The use of on-off keying allows for highly efficient transmitter frontend designs that avoid operation of amplifier stages in a resistive mode, which has the potential of reducing their energy usage by an order of magnitude. Link-level simulations show that this physical layer can deal with typical frontend limitations and can operate in challenging non-line-of-sight channels. For these reasons, we believe that the solution evaluated here can deliver a significant contribution to optical wireless communications technology in a wide range of use cases.**

***Index Terms*—Digital signal processing, LiFi, optical wireless communications, physical layer, pulse modulation, visible light communication, wireless communication.**

I. Introduction

MOST of the existing literature on the physical layer (PHY) for optical wireless communications (OWC) considers downlink transmission from the lighting infrastructure to the mobile device, focusing on high data rates achieved through spectrally efficient modulation. However, systems designed for the Internet of Things (IoT), for example in industrial use cases, need moderate data rates and satisfactory link reliability while operating on battery power. Therefore, a low power design is needed, especially for the uplink. A viable approach to realize link reliability is to use wide-beam transmitters and large-field-of-view receivers that create overlapping areas of service, so that a mobile device always can be reached through multiple access points and a single blocked line of sight does not lead to a link interruption [1], [2]. However, such wide beams cause a distribution of optical power over a larger area, reducing the signal power and with that the signal-to-noise ratio (SNR) at the receiver. Thus, an energy efficient system design is required that is able to work at low SNR levels.

Early investigations of OWC have already considered pulse based and single-carrier modulation techniques, such as variants of pulse position modulation (PPM), on-off keying (OOK), and phase shift keying (PSK) [3]–[5]. Later research then moved on to multi-carrier modulation and has focused on the development of orthogonal frequency-division multiplexing (OFDM)-based concepts, often combined with adaptive bit loading [6]–[10]. OFDM schemes provide some significant advantages, such as high robustness against multipath dispersion, high spectral efficiency, and the ability to adapt to varying channel conditions. Notwithstanding that, with the goal of meeting the demand for low-power IoT solutions, we return to simpler modulation formats and evaluate in this article a complete PHY based on OOK. While OOK enables a near-optimal utilization of available optical power, the core reason for this choice is in the simplified transmitter frontend design, where energy savings are expected to be significant enough to justify the much-increased need for bandwidth due to the low spectral efficiency. This choice will be justified in Section II, starting by pointing out energy efficiency issues of OFDM in OWC and then showing how OOK enables substantial energy savings in transmitter frontends.

The main contribution of this work is to evaluate the complete design of a PHY built on OOK, named the Pulsed Modulation PHY (PM-PHY). This includes assessments of frame synchronization, header and payload detection, and a detailed analysis of the PHY's capability to deal with different channel conditions due to multipath distortion and common analog frontend impairments. These findings stem from two previous publications: The evaluations of the PM-PHY under different channel conditions served as a basis for its definition in IEEE P802.15.13 standardization and were previously presented in [11]. The results considering analog frontend impairments were previously published in [12]. Here we are combining these results into a comprehensive evaluation of the PM-PHY and give a classification of the findings with respect to requirements of future system designs.

The remainder of this article is structured as follows: The expected energy savings through the use of OOK are deduced in Section II. Section III introduces the concepts

Manuscript received December 6, 2019; revised July 27, 2020 and October 16, 2020; accepted November 8, 2020. Date of publication November 17, 2020; date of current version March 18, 2021. This work was supported in part by the German Federal Ministry of Education and Research (BMBF) through the Project SESAM under Grant 16KIS0639K, and in part by the European Union's Horizon 2020 Project ELIOT under Grant 825651. The editor coordinating the review of this article was L. Chiaraviglio. *(Corresponding author: Malte Hinrichs.)*

Malte Hinrichs, Jonas Hilt, Peter Hellwig, Dominic Schulz, Anagnostis Paraskevopoulos, Kai Lennert Bober, Ronald Freund, and Volker Jungnickel are with the Photonics Networks and Systems Department, Fraunhofer Heinrich Hertz Institute, 10587 Berlin, Germany (e-mail: malte.hinrichs@hhi-extern.fraunhofer.de).

Pablo Wilke Berenguer was with the Photonics Networks and Systems Department, Fraunhofer HHI, 10587 Berlin, Germany. He is now with Microsoft Research Cambridge, Cambridge CB1 2FB, U.K.

Digital Object Identifier 10.1109/TGCN.2020.3038692

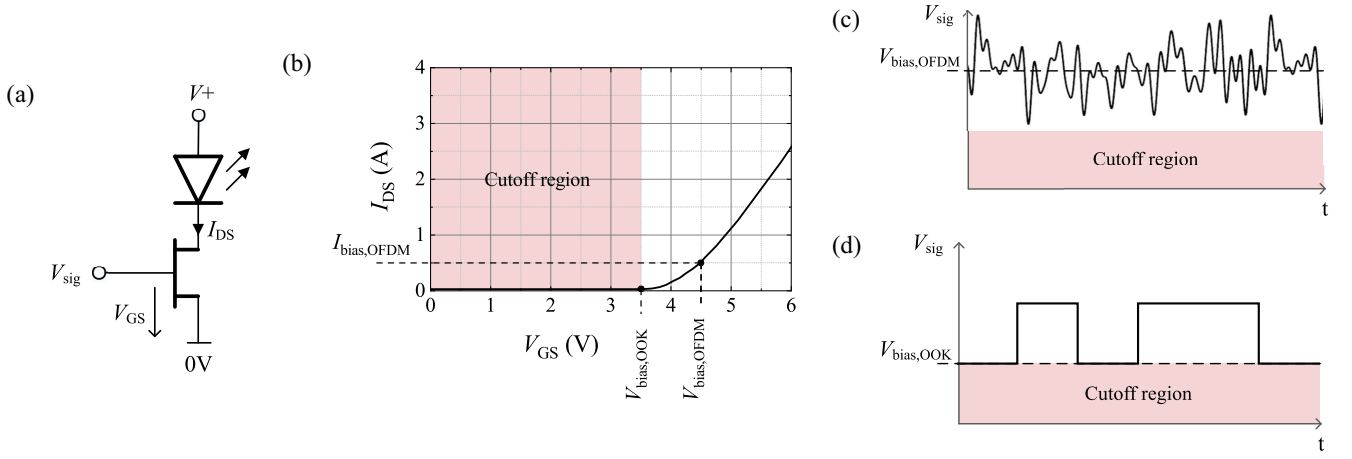

Fig. 1. Visualization of the amplifier bias points for OFDM and OOK modulation in a simplified frontend amplifier model. (a) Amplifier circuit consisting of an LED and a transistor (MOSFET). (b) Exemplary MOSFET output characteristic (drain-source current I_{DS} over gate-source voltage V_{GS}). The cutoff region marks the range for V_{GS} where $I_{\mathrm{DS}} \approx 0$. (c) OFDM and (d) OOK waveforms with required bias voltages relative to cutoff region.

of the PM-PHY in detail. Models and methods used for the performance evaluation are described in Section IV. Section V discusses simulation results and proposes an efficient parametrization for the PM-PHY, and conclusions are drawn in Section VI.

II. Energy Savings in Transmitter Frontends

As stated in Section I, the main energy savings expected from using OOK are achieved in the transmitter frontends, especially in comparison with OFDM. In this section, a simple model of a transmitter frontend is used to quantify these savings.

A challenge for applying OFDM in OWC is that waveforms need to be purely non-negative. This is commonly realized through so-called DC biased optical OFDM (DCO-OFDM), which simply adds a constant bias to the bipolar OFDM signal. While this preserves all the mentioned advantages of OFDM, it introduces a penalty in energy efficiency. In the case of 4-QAM modulated subcarriers, this amounts to 6-7 dB [13], for example. Another issue of OFDM is its high peak-to-average power ratio (PAPR), which increases the required dynamic range for transmitter amplifiers. It also means that a higher peak transmitter power is needed to achieve a certain average power, and accordingly SNR, at the receiver.

Some modifications have been introduced to OFDM, mitigating the need for a constant bias and improving its power efficiency: asymmetrically clipped optical OFDM (ACO-OFDM) [14] and unipolar OFDM (U-OFDM) [15] remove or invert and interleave all negative waveform components at the cost of halving the spectral efficiency. Layered ACO-OFDM (LACO-OFDM) [16] and enhanced U-OFDM (eU-OFDM) [13] build on those concepts and introduce symbol repetitions and addition of multiple signal layers, respectively, to restore the lost spectral efficiency while preserving good power efficiency. However, these layered modulation formats increase receiver complexity and work best at high SNR, which also limits their deployment in networks with a demand for low energy consumption.

A. Linear Transmitter for OFDM Signals

A core issue regarding power efficiency in OWC systems is in the design of linear physical transmitters, especially when using DCO-OFDM. In order to better approach this issue, we regard a simplified transmitter frontend model, shown in Fig. 1a. It consists only of a light-emitting diode (LED) and a transistor, where the LED is connected to the drain connection of the transistor and a signal source is connected to the gate. A supply voltage V_+ is applied between the upper port of the LED and the source port of the transistor is connected to the ground. In this model, the transistor is used as an amplifier modulating the LED through its drain-source current I_{DS}, which changes in dependence on the gate-source voltage V_{GS}, here equal to the signal voltage V_{sig}. Fig. 1b shows the output characteristics for an exemplary metal oxide semiconductor field-effect transistor (MOSFET) used in OWC frontends, driven in the ohmic region at a drain-source voltage $V_{\mathrm{DS}} = 10$ V. Notably, there is a threshold for V_{GS}, below which no current flows through the drain-source connection, and accordingly the LED. This threshold is here around 3.5 V. The region below it is defined as the "cutoff region".

In order to transmit an OFDM waveform, for which Fig. 1c shows an example, a biasing of V_{GS} is mandatory, in order to exceed the threshold for the cutoff region at all signal levels and achieve a satisfactory linearity. This bias ($V_{\mathrm{bias,OFDM}}$ in Figs. 1b and 1c) leads to a constant current flow through the LED and the transistor's drain-source path and thereby to a constant power consumption in the OWC frontend. Note that in this state power is converted both in the LED and in the transistor, as the transistor is not fully switched on and acts as an ohmic load itself. In this mode, the used power is described by (1). Since the MOSFET acts as a resistor that limits the current through the LED at $I_{\mathrm{DS}} = I_{\mathrm{bias,OFDM}}$, the voltage V_+ is relatively constant and the power consumed by the frontend in Fig. 1a, P_{OFDM}, is given by:

$$P_{\mathrm{OFDM}} = I_{\mathrm{bias,OFDM}}\, V_+ \tag{1}$$

Only the contribution caused by the biasing is considered here. Signal variations are not regarded, as most of the signal

power is closely distributed around the average (in this case, the bias), assuming OFDM waveforms with high PAPR. A $V_{\mathrm{bias,OFDM}} = 4.5$ V, which is 1 V above the cutoff threshold, leads to a drain-to source current $I_{\mathrm{bias,OFDM}} = 0.5$ A. With a supply voltage $V_+ = 12$ V, an average power consumption $P_{\mathrm{OFDM}} = 6$ W is estimated for the OFDM case.

B. Switching Transmitter for OOK Signals

For transmission of OOK signals, for which an example is shown in Fig. 1d, linearity is not critical and the bias voltage $V_{\mathrm{bias,OOK}}$ can be placed just at the border of the cutoff region. In this mode, the modulation amplitudes for V_{GS} are selected so that the drain-source current through the transistor is practically switched off for modulation of a "0" (i.e., $V_{\mathrm{GS}} = V_{\mathrm{bias,OOK}}$) and fully on for a "1" ($V_{\mathrm{GS}} \gg V_{\mathrm{bias,OOK}}$). In the "fully on" state, the transistor is not in the ohmic region, so the characteristics in Fig. 1b do not apply. Instead, the resistance between drain and source becomes very small (parameter $R_{\mathrm{DS,on}}$, usually in the order of mΩ). This means that in both of these states very little energy is dissipated in the transistor itself, as it is either blocking or transmitting with minimal resistance most of the time. Practically, the transistor will still operate in the ohmic region during each transition between states, since state changes are not immediate, but the occurrence of this state is minimized through OOK.

The used power in this switching mode is now dominated by the LED energy consumption and given by (2) for the "on" case. Since the transistor resistance is very low, the maximum current needs to be limited outside the shown circuit, e.g., by the voltage source, so that V_+ is not necessarily constant. We now regard the power as the sum of the LED and transistor power. For modulating a "1", we assume that the current I_{DS} is externally limited at I_{LED}, the LED's nominal current. The voltage over the LED is then the forward voltage of the LED $V_{\mathrm{f,LED}}$. As stated above, the transistor in this state has a drain-source resistance of $R_{\mathrm{DS,on}}$. The overall power is then:

$$P_{\mathrm{OOK},1} = I_{\mathrm{LED}}\, V_{\mathrm{f,LED}} + I_{\mathrm{LED}}^2 R_{\mathrm{DS,on}} \tag{2}$$

When transmitting a "0", i.e., $I_{\mathrm{DS}} \approx 0$, practically no current flows and accordingly $P_{\mathrm{OOK},0} \approx 0$. With equal distribution of 0s and 1s, the average used power is then $P_{\mathrm{OOK}} = P_{\mathrm{OOK},1}/2$. Assuming $I_{\mathrm{LED}} = 300$ mA, $V_{\mathrm{f,LED}} = 3$ V, and $R_{\mathrm{DS,on}} = 10$ mΩ, an average power consumption $P_{\mathrm{OOK}} = 450$ mW results.

C. Power Efficiency Comparison

The static energy usage estimated above differs by a factor >12 between the two models. For putting this value in relation to throughput, the effective modulation amplitude needs to be considered, since it determines the achievable SNR at the receiver. As shown in [17], the SNR level needed for a reliable transmission does not vary significantly between single-carrier and multi-carrier modulation if an adequate equalizer is used, but is rather determined by its spectral efficiency. This means that while it could be argued that the higher achievable throughput of OFDM reduces energy usage by shortening the time needed for a given transmission, that advantage fades when taking SNR requirements into account.

In our example, the modulation amplitude for the OFDM signal is derived from the peak-to-peak value of $2I_{\mathrm{bias,OFDM}}$ and the PAPR, for which we have observed 10 as a typical value. The average modulation amplitude without bias is then $2\, I_{\mathrm{bias,OFDM}}/\sqrt{10} = 316$ mA. The modulation amplitude for OOK is given by its peak current $I_{\mathrm{LED}} = 300$ mA, as the balanced OOK signal has a PAPR of 1. The difference between the two transmitters is approx. 5%, which is negligible in the context of this estimate. Thus, both systems can be expected to reach a similar SNR at the receiver and, accordingly, equivalent throughputs. This conversely indicates that in a scenario where the power margin is sufficient for OFDM to achieve a higher spectral efficiency, the OOK system will be able to operate with a lower modulation amplitude, again reducing its energy usage.

These considerations show that the previous comparison of static energy usage serves as an estimate for overall energy efficiency, suggesting that the power used in analog frontends can be significantly reduced by using OOK with transmitter frontends operating in switching mode instead of OFDM. In reality, this gain will be reduced by various parasitic effects of the analog components, but nevertheless we expect a considerable benefit in energy consumption.

III. Pulsed Modulation Physical Layer (PM-PHY)

This section presents the Pulsed Modulation PHY (PM-PHY) as used for our simulations, representing an early version of the corresponding PHY in the IEEE P802.15.13 task group [18]. The components frame synchronization, coding, and frequency domain equalization are separately described.

A. Frame Synchronization

The PM-PHY uses a synchronization preamble structure designed for a detector according to Minn [19], which follows an autocorrelation approach similar to the widely used Schmidl-Cox algorithm [20], but is able to produce a sharper output. This structure is created by repeating a subsequence multiple times with varying signs. The sign pattern determines the shape of the correlator output. At the receiver, this pattern needs to be known, but not the content of the subsequences. Here, a subsequence $\mathbf{A_N}$ of variable length is repeated six times and inverted by the pattern ($+\ +\ -\ +\ -\ -$) to form the vector $\mathbf{A_{prb}} = [\mathbf{A_N}\ \mathbf{A_N}\ \underline{\mathbf{A_N}}\ \mathbf{A_N}\ \underline{\mathbf{A_N}}\ \underline{\mathbf{A_N}}]$, where $\underline{\mathbf{A_N}}$ stands for the inverse of $\mathbf{A_N}$. This preamble structure was recommended in [21].

Binary Gold sequences [22] are used as a base for the subsequences $\mathbf{A_N}$. These are sets of pseudorandom noise (PN) sequences with low bounded cross-correlations between them, designed specifically for spread-spectrum multiplexing systems. They were selected for this particular property, as in the early stages of PHY development a parallel use of several different synchronization sequences was considered for separate purposes. Subsequences with lengths $N_{\mathrm{seq}} = 8,\ 16,\ 32,\ 64$ are considered, so that overall preamble lengths of $N_{\mathrm{prb}} = 48, 96, 192, 384$ result. For each N_{seq}

a maximum length PN-sequence of length $N_{\mathrm{seq}} - 1$, which forms the base for a set of Gold sequences, is appended with a balancing symbol and used as $\mathbf{A_N}$.

B. Coding

Header and payload are evaluated separately by means of the coding schemes defined for the respective frame parts. In the PM-PHY, 8B10B line coding [23] and Reed-Solomon (RS) forward error correction (FEC) [24] are used for both schemes. The header and payload coding schemes differ only by the selected word lengths and redundancies of the RS code, which are described below.

The central component of the coding schemes is the 8B10B line coding. It serves the purpose of ensuring a DC-free transmit signal, which is crucial for modulation in usual high-bandwidth frontends, as their components often exhibit a high-pass characteristic [25].

In order to achieve the desired effect of strictly balancing the analogue signal, the line coding needs to be applied after FEC. Otherwise, the parity bits inserted by the FEC would be transmitted without line coding and introduce a DC-offset again. Applying line coding after FEC, though, deteriorates FEC performance, as even single bit errors can cause up to 5 erroneous output bits in 8B10B decoding. To circumvent this problem, following method is used [18]: Line coding is applied to the data symbols *before* FEC, and again to the parity symbols *after* FEC encoding. Since the RS code is a systematic code, the data symbols pass through the encoder unchanged and their line coding remains intact. At the receiver, this procedure is reversed. First, the line coding of the parity bits is removed, then FEC is decoded, and finally the (now error corrected) line coding of the data symbols is removed. A visualization of this method is given later on in Fig. 5b. To match the length of line-coded data to the word length of the FEC code, zeros are inserted before encoding and removed directly after. This is equivalent to shortening the FEC code, as is also done implicitly by the en- and decoder due to the chosen RS word and parity lengths.

The described method does not completely avoid the drawback of applying 8B10B line coding after FEC encoding, as the parity bits are still line-coded without any error correction, so that bit errors are potentially multiplied on the parity bits. Still, the deteriorative effect is alleviated, as it now only affects the fraction of the transmitted bit stream containing parity symbols. This is confirmed by the results shown in Section V-A2, specifically in Fig. 8.

For header coding, an RS code word with 24 data symbols and 12 parity symbols is defined (RS(36,24)), for payload coding with 248 data symbols and 8 parity symbols (RS(256,248)). Per definition of the Reed-Solomon code, the symbol length for the former configuration is 6 bits and for the latter 9 bits; so the respective code words have lengths of 216 and 2304 bits and contain 144 and 2232 bits of data.[1]

[1]In a later draft of IEEE P802.15.13, generator polynomials have been defined that result in RS symbol lengths of 10 bits. In this work, we use the shortest symbol lengths for the initially given RS configurations.

C. Frequency Domain Equalization

As the PM-PHY is intended to work at high bandwidths up to 200 MHz, channel equalization is required to mitigate frequency selective impairments such as multi-path spreading and band-pass characteristics of physical components. In OFDM-based communication systems, frequency domain equalization (FDE) is commonly applied [6], [10]. This is the obvious choice, as the received signal is transformed to the frequency domain anyway, and each symbol is prepended with a cyclic prefix (CP) to avoid inter-symbol interference. Using reference symbols, the channel can be estimated in the frequency domain by simply dividing the received signal by the known reference symbols. For equalization, the data parts are then multiplied with the inverse of the estimated channel.

For single carrier, and especially pulse amplitude modulation (PAM) based systems such as the PM-PHY, this method requires the artificial creation of a block structure similar to OFDM symbols by inserting CPs in the time domain signals, reducing the throughput [25]. In addition, a dedicated transformation to frequency domain and back to time domain at the receiver is needed, which increases computational complexity. Despite that, the PM-PHY provisions a block structure oriented at the OFDM-based High Bandwidth PHY (HB-PHY), which is also defined in IEEE P802.15.13. Both PHYs use the same block and CP lengths. Eventually, the intention is to create synergies between the PHYs to make them as interoperable as possible and enable combined deployment for up- and downlink, for example. Here, the shortest CP setting from the HB-PHY with a length of 0.16 μs is used. Later versions of the PM-PHY also include a long CP of 1.28 μs, corresponding to the longest HB-PHY setting, which is then mandatory for the header and optional for the payload. The block length without CP is 5.12 μs in all cases. The block and CP lengths in symbols are thus proportional to the symbol rate and the overhead through CP insertion is 1/32 for all symbol rates at the short setting.

IV. Simulation Environment

In this section, the models and methods used for the simulations in this work are presented. First, the models for the optical channel and frontend impairments are introduced. Then, an SNR range for classification of the PM-PHY evaluation results is deduced from a virtual manufacturing hall scenario. Finally, the simulation setups used for the evaluation of frame detection and header/payload coding of the PM-PHY are presented.

These setups were applied both in a wideband and in a narrowband mode. Two optical channel models were used for the evaluation of the PM-PHY in the wideband mode at symbol rates R_{sym} of 50, 100, and 200 MHz, considering FDE and an enhanced frame detection method. The narrowband mode evaluated the PM-PHY at $R_{\mathrm{sym}} = 25$ MHz and focused on the impact of high-pass characteristics in analog optical frontends on low bandwidth PM-PHY signals. Optical channel models and equalization were not regarded in this mode.

All simulations were carried out in MathWorks MATLAB.

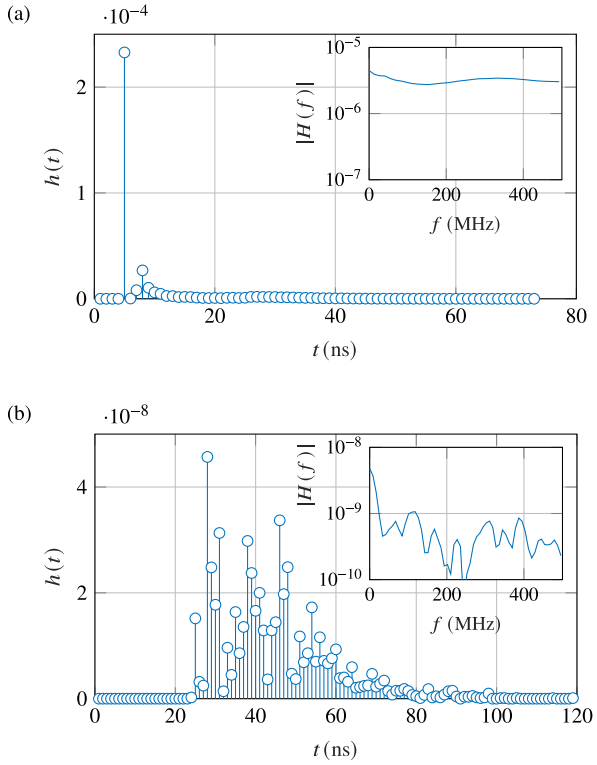

Fig. 2. CIRs of the optical channel models [26]. Insets show magnitude of frequency responses. (a) LOS channel. (b) Multi-path NLOS channel.

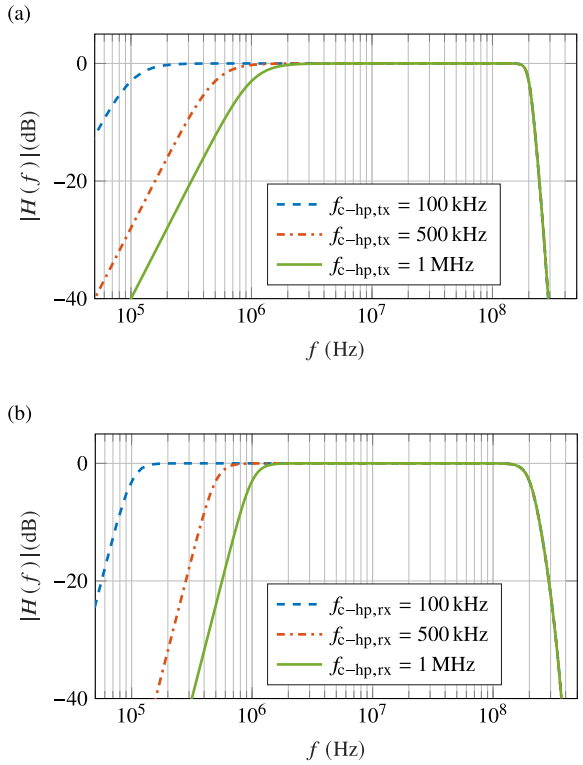

Fig. 3. Magnitude of frequency responses of the optical frontend band-pass models. (a) Tx frontend. (b) Rx frontend.

A. Optical Channel Models

This section describes the two optical channel models that were used for the evaluation of the PM-PHY in the wideband mode. Corresponding channel impulse responses (CIRs) are shown in Fig. 2. The first channel model (Fig. 2a) reflects a line-of-sight (LOS) scenario, the second one a multi-path non-line-of-sight (NLOS) scenario [26]. These models represent exemplary conditions with very different characteristics. For this reason, they also serve as an official evaluation framework in the IEEE P802.15.13 task group [18].

The logarithmic plots in the insets in Fig. 2 show the frequency responses of the regarded channels. The LOS channel has a relatively flat frequency response, while the multi-path channel has a low-pass characteristic with deep fading notches at higher frequencies. This demonstrates the requirement for an FDE especially with the second model.

B. Frontend Models

In physical systems, the signal is influenced by the transmission characteristics of the analog optical frontends (OFEs) on both the transmitter and receiver side. Especially the high-pass characteristic is critical for transmission of the pulsed waveforms of the PM-PHY, since it causes baseline wander and distortion of individual symbols. This effect is most pronounced at low symbol rates, since there are more signal components present at lower frequencies and longer runs of continuous signal states. Accordingly, the PM-PHY is evaluated with the frontend models in the narrowband mode at a symbol rate of 25 MHz.

The OFEs are represented by band-pass filters that were modelled based on actual high-bandwidth prototypes. These models are also used as a reference in IEEE 802.11bb standardization [27]. Their frequency responses are displayed in Fig. 3. The transmitter OFE is modelled using 2th order high- and 8th order IIR low-pass filters (Fig. 3a) and the receiver OFE using 4th order high- and low-pass filters (Fig. 3b). As the models were used to assess the PM-PHY's ability to cope with high-pass filtering, the cut-off frequency $f_{\text{c-hp}}$ of both the transmitter and receiver high-pass components was varied between 100 kHz, 500 kHz, and 1 kHz, corresponding to 0.4, 2, and 4% of the symbol rate. The cut-off frequency of the low-pass was left at 200 MHz, as it is out of the relevant frequency range at the symbol rate regarded here.

C. SNR Range from Multi-Point Transmission Model

In order to evaluate the SNR range in a typical industrial application scenario, a manufacturing hall, described by a geometrical multi-point transmission model, was considered (see Fig. 4). An exemplary arrangement of 12 equally spaced ceiling-mounted transceivers, under which a mobile unit is moving on a specified trajectory, was implemented. In the downlink, the transmitters on the ceiling simultaneously send identical signals to a single receiver on the mobile unit. In the uplink, the signal from the single transmitter on the mobile unit is received by the receivers on the ceiling using equal gain combining. This setup was used to simulate signal strength variations that were then converted to an SNR distribution.

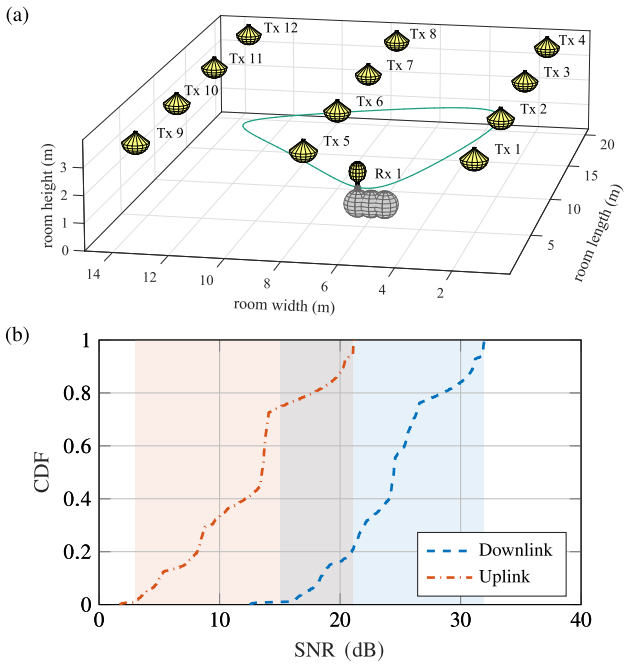

Fig. 4. Manufacturing hall model for SNR range classification. (a) Hall geometry with mobile unit model (grey spheres) and its trajectory (green line). The yellow cones depict fields of view of transmitters (on the ceiling) and receiver (on top of the unit) in the downlink setup. (b) Cumulative distribution of SNR values along the trajectory in downlink and uplink setup. The shaded areas show the range between the 1th and 99th percentiles.

Note that this model is unrelated to the optical channel models presented in Section IV-A. At this stage, ideal LOS connections are regarded that only serve for deriving an SNR operating range for the modelled industrial application scenario.

Fig. 4a shows the geometric setup of the manufacturing hall in the downlink configuration. A cluster of gray spheres is used to model the mobile unit with an upward facing receiver. The transmitters are arranged in a grid on the ceiling. The trajectory of the receiver is marked by a solid green line. The radiation patterns of the transmitters on the ceiling were modelled by a Lambertian function of order 0.5, the sensitivity pattern of the receiver on the mobile unit by one of order 2. These patterns are depicted as yellow cones. In the uplink configuration, transmitter and receiver characteristics are swapped, but the geometry remains the same. Note that the resulting channel is non-reciprocal due to the different optical characteristics of transmitters and receivers. Only LOS channel contributions are considered, as contributions from NLOS detection are typically insignificant and mostly additive to LOS signals at low bandwidth [10].

Using this model, a distribution of SNR values along the mobile unit's trajectory was generated, which is shown in Fig. 4b. The received signal power was calculated from the link distances and angles between transmitters and receivers and their radiation patterns. The noise power was calculated by assuming a fixed noise power per receiver, which was calibrated based on observations from lab experiments. This calibration assumed an SNR of 20 dB for a single link with frontends pointed at each other over a distance of 3 m. The observed SNR values represent the ratio of the accumulated power of all signal and noise components on the receiver side.

The results show that while in the downlink the 1st and the 99th percentile (visualized by the tinted area) are around 15 dB and 32 dB, respectively, in the uplink the SNR values are significantly lower, with the 1st percentile at 3 dB and the 99th at 21 dB. Since equal gain combining was used, this is mainly due to the noise of 12 receivers being added up, instead of noise from only one receiver in the downlink. The 1st percentile values are regarded as SNR thresholds for PHY evaluation in Section V-C.

TABLE I
TABLE OF NOTATION

Symbol	Description	Unit
$\mathbf{A_N}$	Sync. preamble subsequence	a.u.
$\mathbf{A_{prb}}$	Complete sync. preamble	a.u.
$f_{\text{c-hp,tx/rx}}$	Tx/Rx OFE high-pass cut-off freq.	Hz
N_{cw}	Data bits per code word	1
N_{prb}	Sync. preamble length	1
N_{seq}	Preamble subsequence length	1
N_{win}	Sync. averaging window length	1
$r_{\text{dec,hdr/pl}}$	Block dec. success rate of hdr./payload	1
r_{sync}	Preamble detection rate	1
R_{sym}	Symbol rate	Hz
T_{sym}	Symbol duration	s
τ_{max}	Maximum delay spread for sync.	s

D. Simulation Setups

Two simulation setups were implemented in MATLAB to evaluate the synchronization mechanism ("Synchronization setup") and the coding schemes for header and payload ("Coding setup"). Both setups used the same basic method. A transmit signal was passed through a channel or frontend model, additive white Gaussian noise (AWGN) was added to set a specific SNR, and the resulting signal was evaluated. In the following subsections, these setups are presented in detail. Separate subsections describe the channel representation and a parametrization utilizing both setups. Prior to this, the wideband and narrowband operation modes applied in the setups are described.

In the *wideband mode*, the optical channel models (Section IV-A) were applied but not the OFE models (Section IV-B), as the influence of the latter is low at high bandwidths. The PM-PHY was simulated at symbol rates R_{sym} of 50, 100, and 200 MHz. The averaging method to detect the synchronization preamble also in strong multi-path conditions was investigated, and FDE was regarded for header and payload demodulation. For this purpose, CPs were inserted in the data stream. The goal was to assess the PHY's general capability to deal with different channels at large bandwidths.

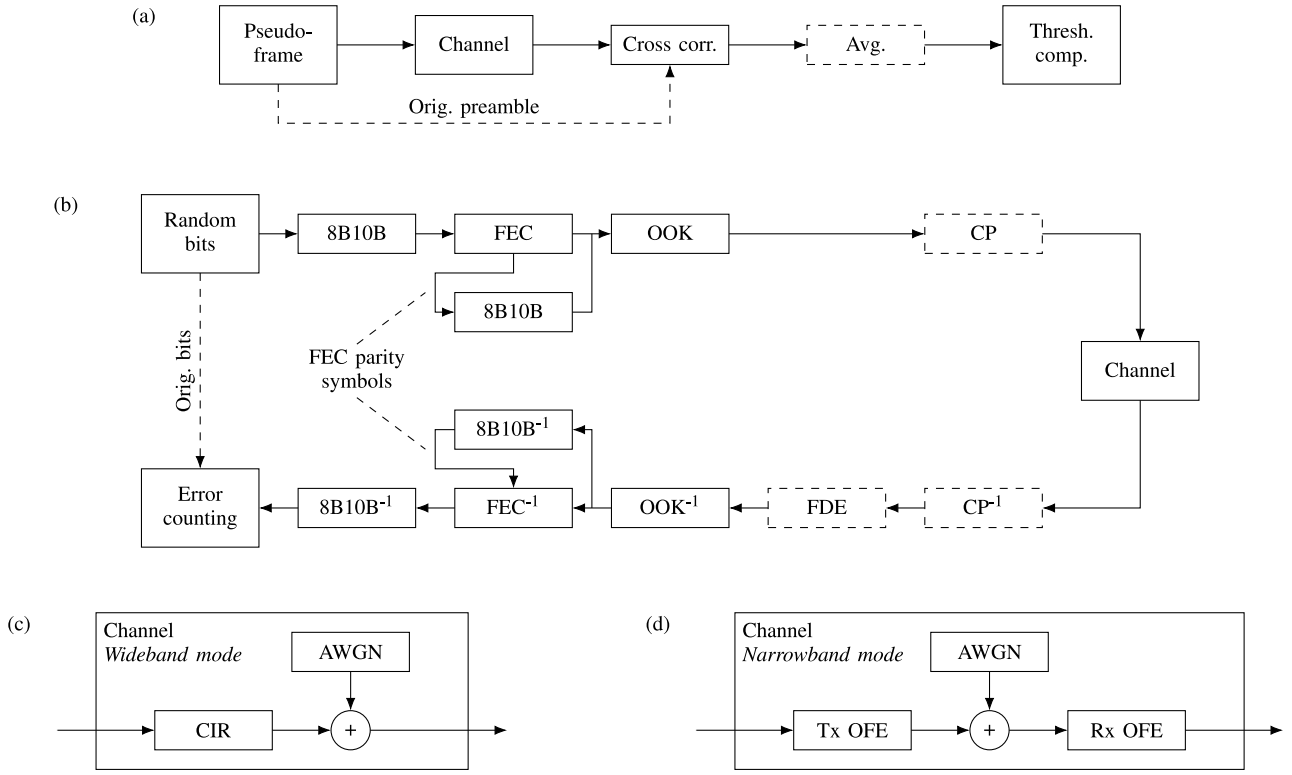

Fig. 5. Simulation block diagrams. Dashed blocks are included only in wideband mode. (a) Frame synchronization evaluation (*Synchronization Setup*). (b) Coding scheme evaluation (*Coding Setup*). (c) Channel simulation block for wideband mode. (d) Channel simulation block for narrowband mode.

In the *narrowband mode*, a low symbol rate of 25 MHz was used and neither the enhancement to frame detection nor FDE were applied. The focus was on investigating the PHY's ability to deal with high-pass characteristics in analog frontends at a low symbol rate, e.g., in a low cost deployment with minimum complexity. At low symbol rates, the impact of the optical channel can be expected to be minimal under LOS conditions (see Section IV-A). For this reason, the OFE models were used here but not the optical channel models.

1) Synchronization Setup: For the evaluation of frame start detection, depicted by the block diagram in Fig. 5a, pseudo frames were constructed, consisting of the preamble vector $\mathbf{A_{prb}}$ (see Section III-A) preceded by zeros and followed by random OOK symbols. These frames were passed through the channel simulation (*Channel* block) at the respective symbol rate. Then the cross correlation was calculated between the received signal and the ideal preamble sequence *(Cross corr.)* and the frame start was detected at the first position where the cross correlation output lay over a detection threshold *(Thresh. comp.)*. The derivation of this threshold is described later on. The whole process was repeated $10,000$ times for each configuration. The dashed box *Avg.* represents an enhancement for the wideband mode simulations that is also described later on. Apart from that, the setup is identical for narrowband and wideband mode.

We selected cross correlation as an approach for frame synchronization, as it is able to produce an even sharper peak than the autocorrelation based detector that the preamble was designed for (see Section III-A). The usual drawback of cross correlation, its high computational complexity, is also alleviated in case of the PM-PHY. Since the preamble sequence is binary and can be represented as either -1 or $+1$, the computationally expensive multiply-and-accumulate operations, which the cross correlation is based on, transform into inversion and addition of the received samples.

Frame synchronization was then achieved by comparing the cross correlation output values to a fixed threshold. The amplitude of this threshold is critical for balancing false positive and false negative detections. If the threshold is too low, false detections are more probable; if it is too high, true frame starts are less likely detected. This detection threshold was derived as follows prior to the simulation: A vector containing $100,000$ random AWGN samples with an average power 5 dB higher than the preamble's signal power was generated. The cross correlation of the preamble with this noise vector was then calculated and the threshold was selected so that 1/1000 of the resulting values lay above the threshold, i.e., a false positive rate of 0.001 resulted for the detector.

Initial simulations showed that for channels with considerable inter-symbol interference (ISI), such as in the NLOS channel presented in Section IV-A, frame detection did not work reliably. This is due to the signal energy being spread out over multiple paths in the channel, which generates a smaller separate peak for each path in the cross correlation output. For this reason, following enhancement was made to the preamble detector in order to enable operation also in those channels: The output from the cross correlation was averaged over a small number of samples, and a corresponding

timing tolerance was defined for the detector output. The desired effect is that the separate correlator output peaks will be summed up while the noise is reduced and a higher relative peak amplitude results. The maximum delay spread acceptable for this technique is given by $\tau_{\max} = N_{\text{win}} * T_{\text{sym}}$, with the number of samples in the averaging window N_{win} and the sampling time $T_{\text{sym}} = 1/R_{\text{sym}}$, with R_{sym} the symbol rate. This method is represented in Fig. 5a by the dashed block '*Avg.*'. Averaging window lengths $N_{\text{win}} = 1, 2, 4, 8$ were considered and a synchronization tolerance of the same length was set. $N_{\text{win}} = 1$ corresponds to the case without averaging.

2) Coding Setup: The simulation setup for header and payload coding schemes is depicted in Fig. 5b. The blocks exclusive to the wideband mode are dashed, the rest is identical between wideband and narrowband mode.

A data stream of 2×10^6 random bits was coded with the coding scheme described in Section III-B. First, 8B10B line coding was applied *(8B10B)*, followed by FEC using the respective RS code *(FEC)*, with a separate line coding of the parity symbols. The resulting bit-stream was modulated to OOK symbols at the selected symbol rate *(OOK)*. Despite the denomination OOK, a bipolar electrical representation of the waveforms was actually used, meaning the OOK symbols were represented as $+1$ and -1. This is justified by the high-bandwidth electrical circuits in physical OFEs usually working in an AC-coupled mode, which converts the unipolar optical waveforms to a bipolar form by removing the DC component. In the wideband mode, CPs were inserted *(CP)* before the signal was passed through the channel simulation *(Channel)*.

On the receiver side, in the wideband mode the CP was removed again *(CP^{-1})* and block wise FDE was carried out *(FDE)* using the frequency domain representations of the ideal CIRs. Then in both modes OOK demodulation *(OOK^{-1})* and decoding of line coding and FEC was done *(8B10B^{-1})*, *(FEC^{-1})*. Reversing the scheme applied in the transmitter path, the line coding of the FEC parity bits was removed separately before FEC decoding. Finally, the received bit stream was compared to the original one and errors were counted *(Error counting)*.

3) Channel Simulation: Fig. 5c shows the channel simulation block used for the wideband mode in the setups described above. The input signal is convolved with a CIR representing one of the channels described in Section IV-A *(CIR)* and then white Gaussian noise is added to the signal *(AWGN)* in order to set a specific SNR.

In the narrowband mode, using the block depicted in Fig. 5d, the incoming signal is first passed through the transmitter frontend model *(Tx OFE)*, as described in Section IV-B. Then AWGN is added and the receiver side frontend model *(Rx OFE)* is applied.

4) Physical Layer Parametrization: Using the setups described above, a parametrization of the synchronization preamble was carried out in the wideband mode. The considerations in narrowband mode had a smaller scope and because of that only regarded one exemplary preamble length. As a goal for parametrization, the preamble should not be too short, as this affects the synchronization performance, but it should also not be arbitrarily long, in order to avoid overhead. To reach the goal of finding the optimal preamble length, the performances of frame synchronization, header coding, and payload coding were put in relation to each other. Accordingly, following guideline was defined: The SNR at which the payload coding scheme reaches a block success rate of $r_{\text{dec,pl}} = 0.9$ should be greater than the SNR at which the header coding scheme reaches a block success rate of $r_{\text{dec,hdr}} = 0.99$, which in turn should be greater than the SNR at which the frame synchronization mechanism reaches a detection rate of $r_{\text{sync}} = 0.999$.

The staggered requirements for the different frame parts ensure that when transmitting full frames, data is not lost due to synchronization or header errors, respectively, where the payload can effectively be demodulated. In that way, this guideline also serves to assess the construction of header and payload coding. The block decoding success rates for header and payload are given by $r_{\text{dec}} = (1 - \text{BER})^{N_{\text{cw}}}$, with BER the bit error rate of the decoded data stream and N_{cw} the number of data bits in a respective FEC word in the PM-PHY coding scheme.

V. Simulation Results

This section presents the results from the simulations with the setups described in Section IV. First, evaluations of the wideband setup are presented. Frame synchronization, coding schemes, and FDE are evaluated and the parametrization of the synchronization preamble is carried out. Then, the results from the narrowband setup are given, also containing an evaluation of frame synchronization and the coding schemes. Finally, the results are briefly discussed in the context of the multi-point model presented in Section IV-C.

A. Wideband Mode

In the following, the results generated in wideband mode are presented. As described before, the wideband mode was evaluated considering optical channel models as well as FDE.

1) Frame Synchronization: Frame synchronization performance was evaluated for transmissions at symbol rates of $R_{\text{sym}} =$ 50, 100, 200 MHz in the LOS channel. For the multi-path channel, frame synchronization enhanced by the averaging method was evaluated for a symbol rate of $R_{\text{sym}} = 200$ MHz.

The preamble sequence length has a large influence on the performance of the frame synchronization algorithm. Fig. 6 gives an overview of the evaluation of different synchronization preambles at $R_{\text{sym}} = 200$ MHz with lengths from $N_{\text{prb}} = 48$ to 384 samples over the LOS channel, where the performance is mainly limited by the AWGN. In Fig. 6a, the detection rate r_{sync} is plotted over SNR, i.e., the average power ratio of the signal after application of the channel model (see Fig. 5c) and the AWGN. For preamble lengths of 96 samples and higher, it can be observed that a doubling of sequence length results in a penalty of about -3 dB. This is to be expected, as twice as many samples are added up and effectively averaged during the cross correlation calculation, canceling out the influence of AWGN, correspondingly. However, the performance decreases more steeply when using

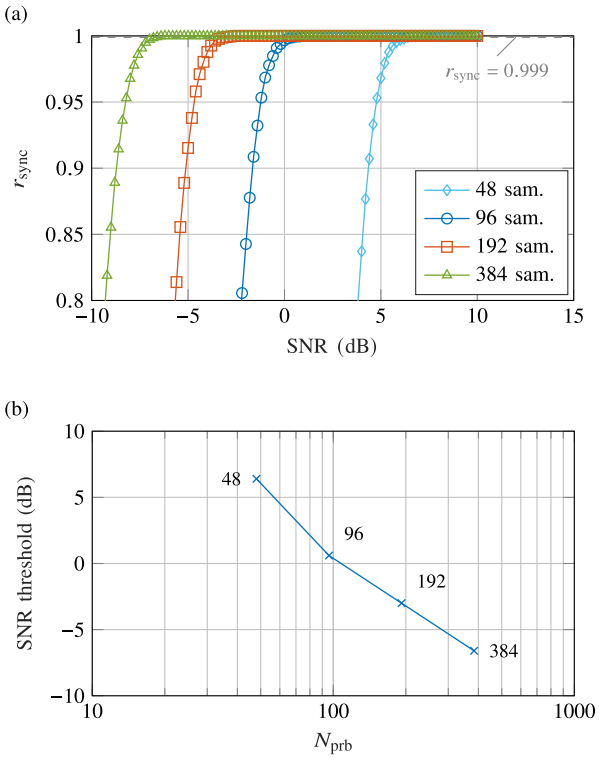

Fig. 6. Sync. performance for LOS channel at $R_{\text{sym}} = 200$ MHz for different preamble lengths N_{prb}. (a) Sync. detection rate over SNR. r_{sync} describes the ratio of synchronization preambles detected at the correct position. (b) SNR threshold for $r_{\text{sync}} \geq 0.999$ over N_{prb}.

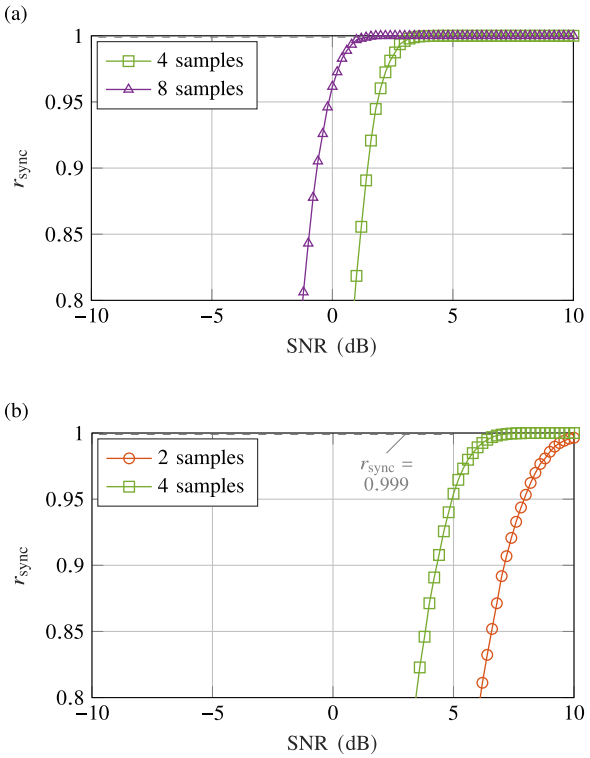

Fig. 7. Sync. detection rate r_{sync} for the multipath channel when enhanced using averaging with different window lengths N_{win} at $R_{\text{sym}} = 200$ MHz with preamble lengths of (a) 96 samples and (b) 48 samples with a lower detection threshold.

a sequence with only 48 samples. Here, the offset from the sequence with 96 samples is around 6 dB. This observation may be explained through side peaks in the autocorrelation of the synchronization preamble, which is made up of six repeated and alternated sequences. Even though the side peaks are intentionally kept low by the repetition pattern, their impact in relation to the main peak increases for shorter sequences, as the influence of noise is larger and the main peak is less distinct.

Fig. 6b shows for each preamble length the SNR, at which the detection rate target of $r_{\text{sync}} = 0.999$ is first exceeded. This graph confirms the decrease of roughly 3 dB for each doubling of synchronization sequence length for 96 samples and above, with a steeper descent between 48 and 96 samples.

Further simulations, for which the results are not displayed here, showed that in the multipath channel the basic synchronization did not work reliably for $\text{R}_{\text{sym}} > 50$ MHz. As described in Section IV-D1, the reason for this is that the output of the cross correlation produces peaks for every signal path in the multi-path channel. Thus, for the multi-path channel the averaging method also described in that section was evaluated and was found to enable operation also at higher rates.

The results at a symbol rate of 200 MHz are shown in Fig. 7. In Fig. 7a, window lengths of 4 and 8 samples are compared for a preamble with $N_{\text{prb}} = 96$ samples. The performance was best for $N_{\text{win}} = 8$, with the penalty relative to the LOS case being less than 2 dB (compare Fig. 6). For a preamble length of 48 samples, the performance threshold could not be reached with any of the regarded window lengths. Since the results indicated that this might be due to the detection threshold being too high, the average power of the noise vector used for the deduction of the threshold (see Section IV-D1) was lowered from 5 to 0 dB relative to the OOK symbols in order to generate a lower threshold. The goal was to find out if under these circumstances the short preamble could also work, as this would save overhead in a real system. The results generated with the corresponding threshold are shown in Fig. 7b. A windowing of 4 samples reached the best performance, with a penalty of less than 1 dB with regard to the LOS case. Window sizes not shown here did not reach the detection rate threshold.

The results show that depending on the preamble length, the frame synchronization method based on cross correlation is able to function reliably even at SNRs < 0 dB in relatively frequency flat channels, which promises robust operation also in low power systems. At maximum symbol rate, a detection rate of $r_{\text{sync}} = 0.999$ is reached between -6.6 dB for the longest and 6.4 dB for the shortest preamble. In the frequency selective multi-path channel, the enhancement based on averaging enabled reliable operation with a low SNR penalty compared to the LOS case.

2) Coding Schemes: An evaluation of the error correction capability through the combined FEC and line coding was performed. As described in Sections III-B and IV-D2, a nested code structure was created in order to minimize error multiplication effects through the necessary line coding. Fig. 8 shows the block error rate (BLER) of the header and payload

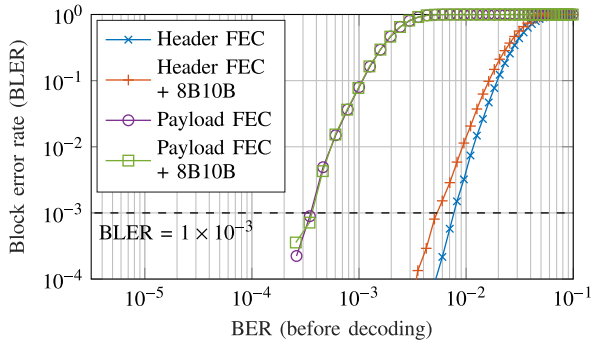

Fig. 8. FEC block error rate (BLER) over bit error rate (BER) of the coded data stream. The BER variation was generated by adding AWGN at different power levels.

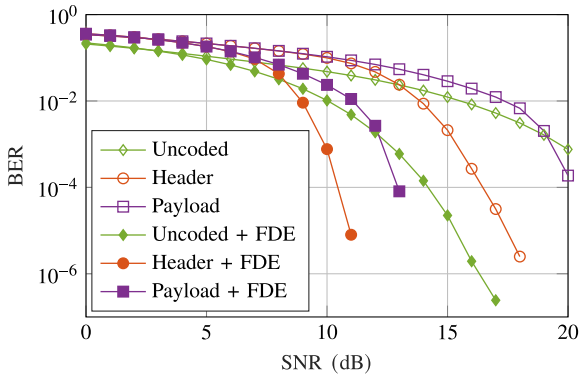

Fig. 9. Performance of header and payload coding schemes over the multi-path channel at $R_{\mathrm{sym}} = 50$ MHz with and without FDE.

coding schemes over a range of input bit error rates (BERs), both with and without 8B10B line coding enabled. The BLER describes the ratio of FEC words still containing at least one bit error after decoding. By putting it in relation to the BER of the received data stream before decoding, a measure for the capability of error correction is provided. The range of different BERs on the received data was produced by adding AWGN at different power levels for this purpose. For setting the performance of the coding schemes in relation, an exemplary BLER threshold of 1×10^{-3} is displayed.

The header coding scheme clearly outperforms the payload coding scheme. The BLER threshold is achieved around a BER of 3×10^{-4} for the payload, and at over an order of magnitude higher for the header around 5×10^{-3}. This is due to the much higher redundancy of the FEC used in the header coding scheme (code rate 2/3) compared to the one used for the payload (code rate 31/32). The error multiplication effect of 8B10B line coding becomes visible in the performance of the header coding scheme, but the impact is minor. It is barely visible for the payload coding, due to the portion of parity bits not protected through FEC and the absolute BER being much lower. These results validate the nested code design and confirm that header decoding is reliable whenever the payload can be decoded.

3) Frequency Domain Equalization: The coding schemes were again evaluated with and without FDE. Since the impact of FDE was marginal in the LOS channel, only the results for the multi-path channel are shown in Fig. 9. The output BERs of the uncoded data stream, a data stream encoded with the header coding scheme, and a data stream encoded with the payload coding scheme are set in relation to SNR. A symbol rate of 50 MHz was selected here to enable a comparison to the transmission without FDE, which did not produce useful results at higher rates.

Note that due to the number of 2×10^6 bits used for the simulation, error-free transmission was observed at SNRs with an actual BER below approx. 1×10^{-6}, which means the measured BER appeared as 0. This cannot be displayed in the plots due to the logarithmically scaled y-axes, so they end at the last SNR where errors were still observed. The simulated SNR range was identical for all plots, nonetheless.

Due to its better error correction capability (see Fig. 8), the header coding scheme achieved error-free transmission at a lower SNR than the payload coding scheme. Without FDE, it was reached for the header at SNRs above 18 dB, whereas the payload and the uncoded stream did not reach error-free transmission in the regarded range. Applying FDE showed a large impact. Error-free transmission was then achieved above 11 and 13 dB for header and payload, respectively. The uncoded transmission was error free at an SNR of 18 dB. This shows that in combination with FDE the payload coding provides a significant benefit, lowering the SNR threshold by 4 dB despite its relatively low redundancy.

These results confirm that FDE enables transmission for the PM-PHY in frequency-selective channels even with strong inter-symbol interference.

4) Parametrization of the Synchronization Preamble: In the last step, results from frame synchronization and header and payload coding evaluations were set in relation to each other in order to assess the ability of the PM-PHY to transmit data reliably and to find the optimal synchronization preamble length. The highest defined symbol rate $R_{\mathrm{sym}} = 200$ MHz was selected for this evaluation.

Based on the previous results, for the simulations in the LOS channel neither FDE nor averaging were necessary, i.e., $N_{\mathrm{win}} = 1$. Fig. 10a shows the corresponding results. The points where r_{sync}, $r_{\mathrm{dec,hdr}}$, and $r_{\mathrm{dec,pl}}$ first exceeded their respective thresholds, according to the guideline defined in Section IV-D4, are marked at 6.4, 8, and 10.4 dB. The last of these values can serve as a threshold for reliable operation of the whole PHY. A synchronization preamble length of 48 samples has been selected here, as the performance was already sufficient to meet the required criteria.

For the multi-path channel, FDE and the enhanced synchronization were applied. The results are displayed in Fig. 10b. Two plots are included for the evaluation of frame synchronization with different detection thresholds as shown in Section V-A1. The results for a preamble of 96 samples with a windowing of 8 samples are marked with 'Synchr. a)'. 'Synchr. b)' denotes the results for the preamble of 48 samples and a windowing of 4 samples with a lower detection threshold. Again, the points where the detection and block success rates exceeded their thresholds are marked. They appear at

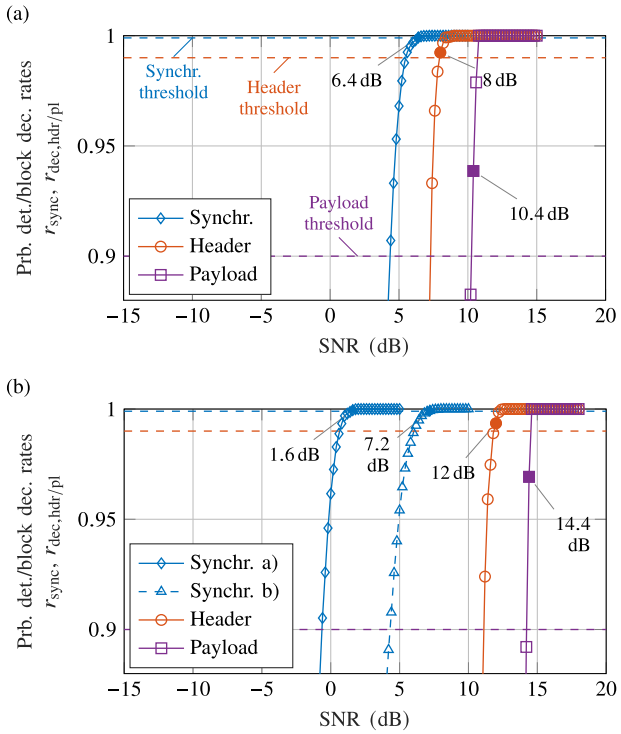

Fig. 10. Detection and decoding rates of frame detector, header, payload encoding for $R_{\text{sym}} = 200$ MHz. (a) LOS channel. (b) Multi-path channel.

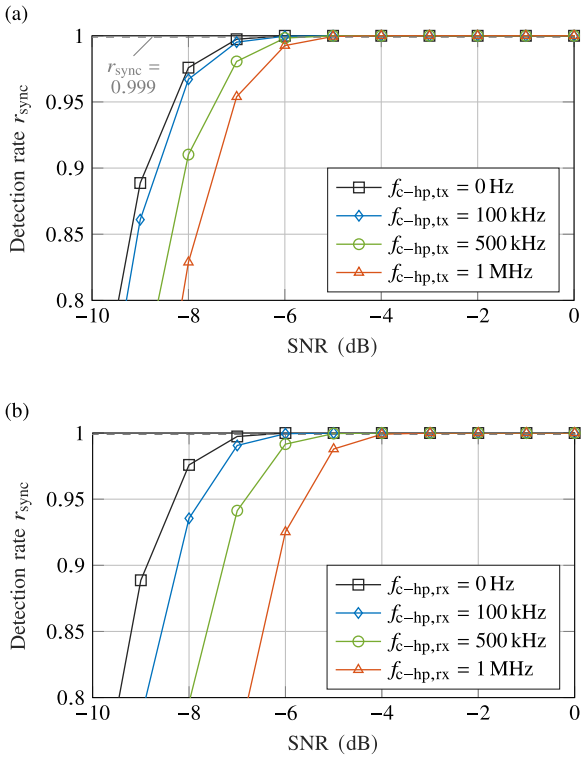

Fig. 11. Frame synchronization performance for different (a) Tx OFE and (b) Rx OFE frequency responses.

1.6, 7.2, 12, and 14.4 dB, showing that for both variants of frame detection the set guideline for reliable operation is safely achieved.

Finally, the results presented above give an SNR range in which the complete PHY operates reliably. For the frequency flat LOS channel model, this range is $\geq$ 10.4 dB; for the strongly frequency selective multi-path channel model it is $\geq$ 14.4 dB.

B. Narrowband Mode

The narrowband mode of the PM-PHY layer was evaluated in a similar way as the wideband mode. For these simulations, a low symbol rate $R_{\text{sym}} = 25$ MHz was used. The impact of the high-pass characteristic of the OFEs was assessed at cut-off frequencies 100, 500, and 1000 kHz, corresponding to 0.4, 2, and 4% of the symbol rate.

1) Frame Synchronization: As for the wideband mode, frame synchronization was evaluated by the preamble detection rate r_{sync} over SNR level, in this case for different high-pass cut-off frequencies. The longest preamble with a length of 384 samples was regarded. Fig. 11 shows the performance for different cut-off frequencies for the transmitter side model (Fig. 11a) and the receiver side model (Fig. 11b). A cut-off frequency of 0 Hz denotes the reference simulation without the frontend model.

With the Tx OFE, the detection rate threshold $r_{\text{sync}} = 0.999$ (see Section IV-D4) is reached at -6 dB for $f_{\text{c-hp,tx}} = 0$ and 100 kHz, and at -5 dB for $f_{\text{c-hp,tx}} = 500$ kHz and 1 MHz. While with the Rx OFE the threshold is reached at similar values, the graph shows that the deterioration at lower SNR is larger. Possible explanations for this are the "coloration" of the noise in the case of filtering on the Rx side, which does not occur for the Tx side filter, and the higher order of the high-pass filter in the Rx side model (see Section IV-B), causing a steeper decline of power towards low frequencies.

Notably, in all configurations the synchronization mechanism achieved the detection rate threshold for an SNR of -4 dB or less, which shows that the frame synchronization is robust against the impact of high-pass filtering at up to 4% of the symbol rate.

2) Coding Schemes: Similar evaluations as in the wideband setup were carried out for the header and payload coding schemes, applying the frontend models at different cutoff frequencies at a symbol rate of 25 MHz. In Fig. 12, the impact of the OFE model on the output BER is shown for header and payload coding with different cut-off frequencies. As with the frame synchronization, it is visible that filtering on the receiver side (Fig. 12a) has a larger impact on the BER than on the transmitter side (Fig. 12b). While the plots for OFEs with a cut-off frequency of 100 kHz barely deviate from the reference simulation (0 Hz), the impact is more clearly visible for frequencies $>$ 100 kHz.

Similar to the results shown in Section V-A3, due to the number of 2×10^6 bits used for the simulation, error-free transmission (found BER $= 0$) was observed at SNRs with an actual BER below approx. 1×10^{-6}. Since this cannot be displayed on the logarithmically scaled y-axis, the corresponding plots end at the last point where errors were still observed. The simulated SNR range was here, too, identical for all shown plots.

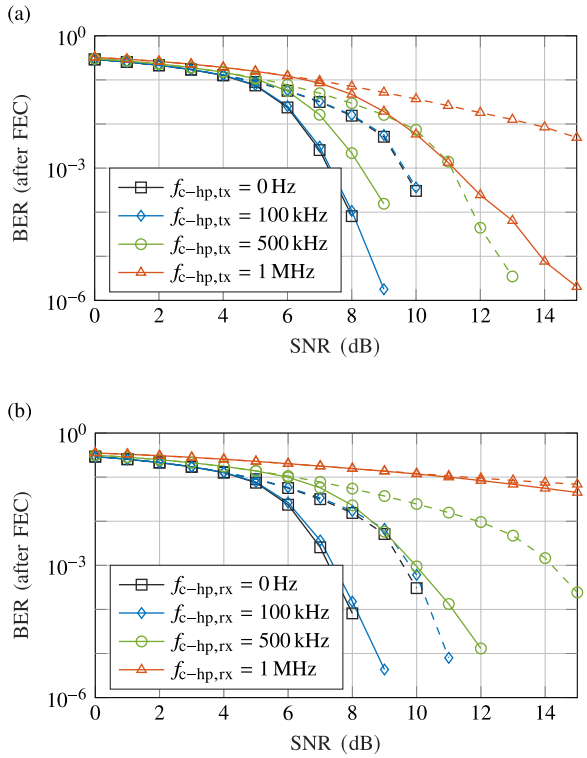

Fig. 12. Header (solid lines) and payload (dashed lines) coding performance for different (a) Tx OFE and (b) Rx OFE frequency responses.

C. Application in a Multi-Point Scenario

In Section IV-C, an exemplary model of a manufacturing hall was used to generate SNR ranges for a typical industrial communication scenario. Putting the results from the previous sections in relation to these ranges delivers valuable insights:

The SNR range for downlink operation with a single receiver starts at 15 dB, whereas the PM-PHY could operate reliably in wideband mode at SNR $\geq$ 10.4 dB in the LOS scenario and at SNR $\geq$ 14.4 dB in the multi-path scenario. This indicates that the PM-PHY will work reliably both in frequency-flat channels and in channels with strong reflective (non-line of sight) components at a high bandwidth. The same is valid in the narrowband setup when high-pass OFE models with cut-off frequencies of 100 kHz and less are used. As shown previously, in this case data transmission was possible at an SNR of 12 dB. Thus, all these configurations can be expected to operate in the regarded downlink setup.

In the uplink setup, however, the SNR range starting at 3 dB exceeds the reliable operative ranges of the PM-PHY in all tested modes and scenarios. As mentioned earlier, the main reason for this low SNR limit is the equal gain combining considered for the uplink of the manufacturing hall model, which causes the received signal to be affected by the noise generated in all 12 receivers. Hence, a reduction of the number of receivers can be expected to relax this limit decisively. An efficient measure to enable PM-PHY operation also with the large number of receivers would be to replace equal gain combining by an adaptive method such as maximum ratio or selection combining [28], [29].

Another approach would be to repeat PM-PHY signals and average the received copies in order to reduce the noise power, effectively increasing the SNR by the repetition factor. For example, in order to reach the SNR limit in the wideband LOS case at 10.4 dB, averaging over 6 repetitions would be necessary, which would correspond to an improvement of the SNR by 7.8 dB. This clearly represents a significant overhead, which might however be acceptable for the uplink in some systems, especially when adaptive re-transmissions are used.

Finally, the comparison with the manufacturing hall model as a reference showed that in a medium sized network using 12 access points, operation in the downlink can be expected to work reliably, whereas the uplink requires either additional overhead or an adaptive combining method.

VI. Conclusion

A complete physical layer based on on-off keying modulation, called the Pulsed Modulation PHY, was evaluated, taking into account the influence of various channel effects. Due to the low peak-to-average power ratio of on-off keying, the same signal-to-noise ratio can be reached at a lower peak transmitter power compared to orthogonal frequency-division multiplexing. A decisive advantage is that with on-off keying, switching transistors can be used in the LED driver, while a linear driver is otherwise needed. An estimation based on a simple model, taking into account the same throughput and the same average modulation amplitudes, quantified power savings of one order of magnitude in the LED driver, which is particularly useful in battery-driven devices.

The physical layer components were assessed in simulations by means of the success rates of frame detection at different preamble lengths and header and payload decoding, applying different channel impairments. The impact of exemplary optical channels was regarded in a wideband mode at symbol rates up to 200 MHz. High-pass filtering common in analog frontends was simulated in a narrowband mode at a symbol rate of 25 MHz. The simulation results have shown that the Pulsed Modulation PHY has the potential of enabling on-off keying based optical wireless communications at all regarded symbol rates, even under difficult channel conditions. Based on a guideline considering frame detection, header, and payload decoding success rates, we found signal-to-noise ratio thresholds of 10.4 dB in a line-of-sight channel and 14.4 dB in a frequency-selective multi-path channel. Considering the high-pass characteristics of the optical frontends, a limit for the cut-off frequency in the order of 2% of the symbol rate was found for reliable operation. The presented results provide detailed insights into the performance of the Pulsed Modulation PHY in IEEE Std. 802.15.13 and give a prospect of future applications for optical wireless communications systems in an industrial context.

Appendix

The frequency domain equalization used here is based on the following algorithm. The input vector $\mathbf{r}$ is split up into blocks of length $N_{\mathrm{blk}} + N_{\mathrm{cp}}$. The block length N_{blk} and

CP length N_{cp} in symbols depend on the symbol rate, since the block and CP durations are constant for all rates (see Section III). From each block a window of N_{blk} samples $\mathbf{s_m}$, starting a few samples before the end of the CP, is selected and transformed to the frequency domain by fast Fourier transform, resulting in the frequency domain representation $\mathbf{S_m}$.

The known channel impulse response $\mathbf{h}$ is extended with zeros to a length of N_{blk} and also transferred to the frequency domain, resulting in the frequency response $\mathbf{H}$. The equalizer coefficients $\mathbf{W}$ are then calculated using the minimum mean square error (MMSE) criterion $\mathbf{W}(n) = \overline{\mathbf{H}}(n)/(|\mathbf{H}(n)|^2 + \sigma_{\mathrm{n}}^2)$, with $n = 1..N_{\mathrm{blk}}$ and the noise variance σ_{n}^2. Equalization is then carried out by calculating $\mathbf{S_m^{eq}}(n) = \mathbf{S_m}(n) \cdot \mathbf{W}(n)$. The result is transferred back to time domain by inverse fast Fourier transform and the equalized signal vector $\mathbf{s_m^{eq}}$ results. The vectors $\mathbf{s_m^{eq}}$ for all blocks are concatenated to form the equalized received signal vector $\mathbf{r^{eq}}$ without CPs.

ACKNOWLEDGMENT

The authors are grateful to their colleagues in IEEE P802.15.13 for discussions and assistance with this work.

REFERENCES

[1] P. W. Berenguer *et al.*, "Optical wireless MIMO experiments in an industrial environment," *IEEE J. Sel. Areas Commun.*, vol. 36, no. 1, pp. 185–193, Jan. 2018.

[2] P. W. Berenguer *et al.*, "Real-time optical wireless mobile communication with high physical layer reliability," *J. Lightw. Technol.*, vol. 37, no. 6, pp. 1638–1646, Mar. 15, 2019.

[3] F. R. Gfeller and U. Bapst, "Wireless in-house data communication via diffuse infrared radiation," *Proc. IEEE*, vol. 67, no. 11, pp. 1474–1486, Nov. 1979.

[4] J. M. Kahn and J. R. Barry, "Wireless infrared communications," *Proc. IEEE*, vol. 85, no. 2, pp. 265–298, Feb. 1997.

[5] R. T. Valadas, A. R. Tavares, A. M. de Oliveira Duarte, A. C. Moreira, and C. T. Lomba, "The infrared physical layer of the IEEE 802.11 standard for wireless local area networks," *IEEE Commun. Mag.*, vol. 36, no. 12, pp. 107–112, Dec. 1998.

[6] O. González, R. Pérez-Jiménez, S. Rodríguez, J. Rabadán, and A. Ayala, "OFDM over indoor wireless optical channel," *IEE Proc. Optoelectron.*, vol. 152, no. 4, p. 199, 2005.

[7] O. González, R. Pérez-Jiménez, S. Rodríguez, J. Rabadán, and A. Ayala, "Adaptive OFDM system for communications over the indoor wireless optical channel," *IEE Proc. Optoelectron.*, vol. 153, no. 4, pp. 139–144, Aug. 2006.

[8] J. Vučič, C. Kottke, S. Nerreter, K.-D. Langer, and J. W. Walewski, "513 Mbit/s visible light communications link based on DMT-modulation of a white LED," *J. Lightw. Technol.*, vol. 28, no. 24, pp. 3512–3518, Dec. 15, 2010.

[9] S. Dimitrov, S. Sinanovic, and H. Haas, "Clipping noise in OFDM-based optical wireless communication systems," *IEEE Trans. Commun.*, vol. 60, no. 4, pp. 1072–1081, Apr. 2012.

[10] P. W. Berenguer, V. Jungnickel, and J. K. Fischer, "The benefit of frequency-selective rate adaptation for optical wireless communications," in *Proc. Int. Symp. Commun. Syst. Netw. Digit. Signal Process. (CSNDSP)*, Jul. 2016, pp. 1–6.

[11] M. Hinrichs *et al.*, "Pulsed modulation PHY for power efficient optical wireless communication," in *Proc. IEEE Int. Conf. Commun. (ICC)*, Shanghai, China, May 2019, pp. 1–7.

[12] M. Hinrichs, P. W. Berenguer, R. Freund, and V. Jungnickel, "Advanced physical layer design for Li-Fi in the industrial Internet of Things," in *Proc. OSA Adv. Photon. Congr. (AP)*, 2019, Art. no. SpTh3E.4.

[13] D. Tsonev, S. Videv, and H. Haas, "Unlocking spectral efficiency in intensity modulation and direct detection systems," *IEEE J. Sel. Areas Commun.*, vol. 33, no. 9, pp. 1758–1770, Sep. 2015.

[14] J. Armstrong and A. Lowery, "Power efficient optical OFDM," *Electron. Lett.*, vol. 42, no. 6, p. 370, 2006.

[15] D. Tsonev, S. Sinanovic, and H. Haas, "Novel unipolar orthogonal frequency division multiplexing (U-OFDM) for optical wireless," in *Proc. IEEE 75th Veh. Technol. Conf. (VTC Spring)*, May 2012, pp. 1–5.

[16] A. J. Lowery, "Comparisons of spectrally-enhanced asymmetrically-clipped optical OFDM systems," *Opt. Exp.*, vol. 24, no. 4, pp. 3950–3966, Feb. 2016.

[17] D. Falconer, S. L. Ariyavisitakul, A. Benyamin-Seeyar, and B. Eidson, "Frequency domain equalization for single-carrier broadband wireless systems," *IEEE Commun. Mag.*, vol. 40, no. 4, pp. 58–66, Apr. 2002.

[18] WPAN Task Group 13, *Multi-Gigabit/s Optical Wireless Communications*, IEEE Standard 802.15, 2017. Accessed: Nov. 11, 2020. [Online]. Available: http://www.ieee802.org/15/pub/TG13.html

[19] H. Minn, V. K. Bhargava, and K. B. Letaief, "A robust timing and frequency synchronization for OFDM systems," *IEEE Trans. Wireless Commun.*, vol. 24, no. 5, pp. 822–839, May 2003.

[20] T. M. Schmidl and D. C. Cox, "Robust frequency and timing synchronization for OFDM," *IEEE Trans. Commun.*, vol. 45, no. 12, pp. 1613–1621, Dec. 1997.

[21] K. Goroshko, K. Manolakis, L. Grobe, and V. Jungnickel, "Low-latency synchronization for OFDM-based visible light communication," in *Proc. IEEE Int. Conf. Commun. Workshop (ICCW)*, London, U.K., Jun. 2015, pp. 1327–1332.

[22] R. Gold, "Optimal binary sequences for spread spectrum multiplexing (corresp.)," *IEEE Trans. Inf. Theory*, vol. IF-13, no. 4, pp. 619–621, Oct. 1967.

[23] A. X. Widmer and P. A. Franaszek, "A DC-balanced, partitioned-block, 8B/10B transmission code," *IBM J. Res. Develop.*, vol. 27, no. 5, pp. 440–451, Sep. 1983.

[24] I. S. Reed and G. Solomon, "Polynomial codes over certain finite fields," *J. Soc. Ind. Appl. Math.*, vol. 8, no. 2, pp. 300–304, Jun. 1960.

[25] L. Grobe, V. Jungnickel, K.-D. Langer, M. Haardt, and M. Wolf, "On the impact of highpass filtering when using PAM-FDE for visible light communication," in *Proc. IEEE Wireless Commun. Netw. Conf. Workshops (WCNCW)*, Apr. 2016, pp. 239–245.

[26] M. Uysal, T. Baykas, F. Miramirkhani, N. Serafimovski, and V. Jungnickel, *TG7r1 Channel Model Document for High-Rate PD Communications*, document P802.15-15-0746–01-007a, IEEE, Piscataway, NJ, USA, Sep. 2015.

[27] M. Hinrichs, J. Hilt, P. Hellwig, V. Jungnickel, and K. L. Bober, *Optical Frontend Model*, document 11–19/0087r1, IEEE 802.11bb Task Group, Piscataway, NJ, USA, Jan. 2019. Accessed: Nov. 11, 2020. [Online]. Available: https://mentor.ieee.org/802.11/dcn/19/11–19-0087–01-00bb-optical-frontend-model-for-phy-simulation.docx

[28] D. G. Brennan, "Linear diversity combining techniques," *Proc. IRE*, vol. 47, no. 6, pp. 1075–1102, Jun. 1959.

[29] J. H. Winters, "Optimum combining in digital mobile radio with cochannel interference," *IEEE J. Sel. Areas Commun.*, vol. SAC-2, no. 4, pp. 528–539, Jul. 1984.

Malte Hinrichs (Member, IEEE) received the B.Eng. degree in electrical engineering from Duale Hochschule Baden–Württemberg Mannheim in 2012, and the M.Sc. degree in electrical engineering from Technische Universität Berlin in 2017, where he is currently pursuing the Dr.-Ing. degree. He has been with Fraunhofer HHI, since 2015, where he joined the Department on Photonics Networks and Systems, and holds a position with Technische Universität Berlin, since 2017. His research interests cover signal processing for energy efficient and robust OWC systems. He is a Member of the Verband der Elektrotechnik Elektronik Informationstechnik.

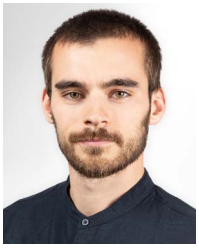

Pablo Wilke Berenguer received the M.Sc. degree in electrical engineering from Stanford University, Stanford, CA, USA, in 2012, and the Dr.-Ing. degree in electrical engineering from Technische Universität Berlin, Berlin, Germany, in 2019. Since 2020, he is a Researcher with Microsoft Research Cambridge. From 2012 to 2020, he was a Research Associate with the Fraunhofer Institute for Telecommunications, Heinrich Hertz Institute, Berlin, Germany. His research interests include digital signal processing and design of optical communication systems, including the mitigation of nonlinear impairments of transmitter components and multiuser MIMO processing in optical wireless communications. More recent interests lie in the field of optical storage technologies. He is a Member of the Verband der Elektrotechnik Elektronik Informationstechnik.

Jonas Hilt received the Diploma degree in electrical engineering from the Berlin University of Applied Sciences, Berlin, Germany, in 2009. In 2009, he joined the Fraunhofer Institute for Telecommunications, Heinrich Hertz Institute, where he is currently an Electrical Engineer with the Department of Photonic Networks and Systems. His current activities include the area of design and realization of embedded systems and visible light communication systems.

Peter Hellwig received the Diploma degree in electrical engineering from the Berlin University of Applied Sciences, Berlin, Germany, in 2009. In 2016, he joined the Fraunhofer Institute for Telecommunications, Heinrich Hertz Institute, where he is currently an Electrical Engineer with the Department of Photonic Networks and Systems. His current activities include the area of design and realization of visible light communication systems.

Dominic Schulz received the M.Eng. degree in communications engineering from the Berlin University of Applied Sciences in 2012, and the Ph.D. degree from Technische Universität Berlin in 2019. He joined the Department of Photonic Networks and Systems, Fraunhofer Institute for Telecommunications, Heinrich Hertz Institute in 2012. He is currently working in the field of optical wireless communications. His current activities include the development of high data rate systems for wireless access, as well as research towards short-range outdoor backhaul links for small radio cells and wireless-to-the-home.

Anagnostis Paraskevopoulos (Member, IEEE) received the Electrical Engineering degree from Technical University, Athens, and the Ph.D. degree from Université Paris–Orsay, with a study on RF modulation of semiconductor lasers performed in the CNET (Research Center-France Telecom), Paris. He joined HHI in 1988, and was since involved in various research projects, including the ESPRIT263 Project on HBTs, a National Project on VCSEL devices at 980 nm in the early 90s, and custom designed laser diodes for non-telecom applications. Over the years, he has successfully coordinated Research and Development Projects, concerning both research subjects and industrial applications. He has authored and coauthored more than 50 scientific papers. His current focus involves applications for optical wireless communication—LiFi.

Kai Lennert Bober received the M.Eng. degree in computer engineering from the Technical University of Berlin in 2018, and joined the Department of Photonic Networks and Systems, Fraunhofer Institute for Telecommunications, Heinrich Hertz Institute in 2016. He is currently working in the field of optical wireless communications at the system level. His current activities include the development of prototypes and research towards realization aspects of distributed MIMO LiFi systems. He also serves as the Technical Editor of the IEEE P802.15.13 Task Group on Multi-Gigabit per Second Optical Wireless Communications.

Ronald Freund received the Dipl.-Ing. degree and the Dr.-Ing. degree "On Computer Aided Modelling of Photonic Systems and Networks" in electrical engineering from the Technical University of Ilmenau (TUI), Ilmenau, Germany, in 1993 and in 2002, respectively, and the MBA degree from RWTH Aachen, Aachen, Germany.

From 1993 to 1995, he worked as a Research Fellow with TUI. In 1997, he co-founded VPI Systems, Inc., formally Broadband Network Design GmbH, where he was involved as a Chief Technology Officer and a Consultant, responsible for the development of design software for the physical layer of photonic networks as well as national and international research assignments. Since 1995, he is with Heinrich Hertz Institute, Berlin, Germany, where he is currently leading the Department Photonic Network and Systems with the focus on the following research areas: Network design and modelling, high-capacity submarine and core networks, high-speed access networks as well as satellite and quantum communication systems. He has authored/coauthored more than 150 scientific publications. In 2017, he has been appointed as a Professor for Photonic Communication Systems with the Technical University of Berlin, Berlin.

Volker Jungnickel (Member, IEEE) received the Doctoral degree in physics from Humboldt University, Berlin, in 1995, and the Habilitation degree in communications engineering from Technical University, Berlin, in 2015. He joined Fraunhofer HHI in 1997, working on optical wireless communications, multiple antenna techniques in mobile networks, and fixed access network infrastructures. Besides, he serves as a Privatdozent with Technical University, Berlin, with lectures and supervises Masters and Ph.D. theses. He serves as the Chair of IEEE P802.15.13 Task Group on Multi-Gigabit per Second Optical Wireless Communications and as a Technical Editor for the IEEE P802.11bb Task Group on Light Communications.